Journal Pre-proof

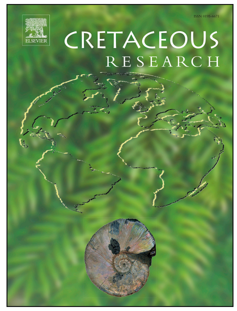

An integrated multi-proxy study of cyclic pelagic deposits from the north-western Tethys: the Campanian of the Postalm section (Gosau Group, Austria)

E. Wolfgring, M. Wagreich, J. Hohenegger, K. Böhm, J. Dinarès Turell, S. Gier, B. Sames, C. Spötl, S.D. Jin

PII: S0195-6671(20)30391-8

DOI: https://doi.org/10.1016/j.cretres.2020.104704

Reference: YCRES 104704

To appear in: *Cretaceous Research*

Received Date: 29 April 2020

Revised Date: 14 October 2020

Accepted Date: 7 November 2020

Authors statement

All authors have contributed to the Conceptualization, Methodology, Investigation, Visualization, and Writing of the manuscript, and approved the final version.

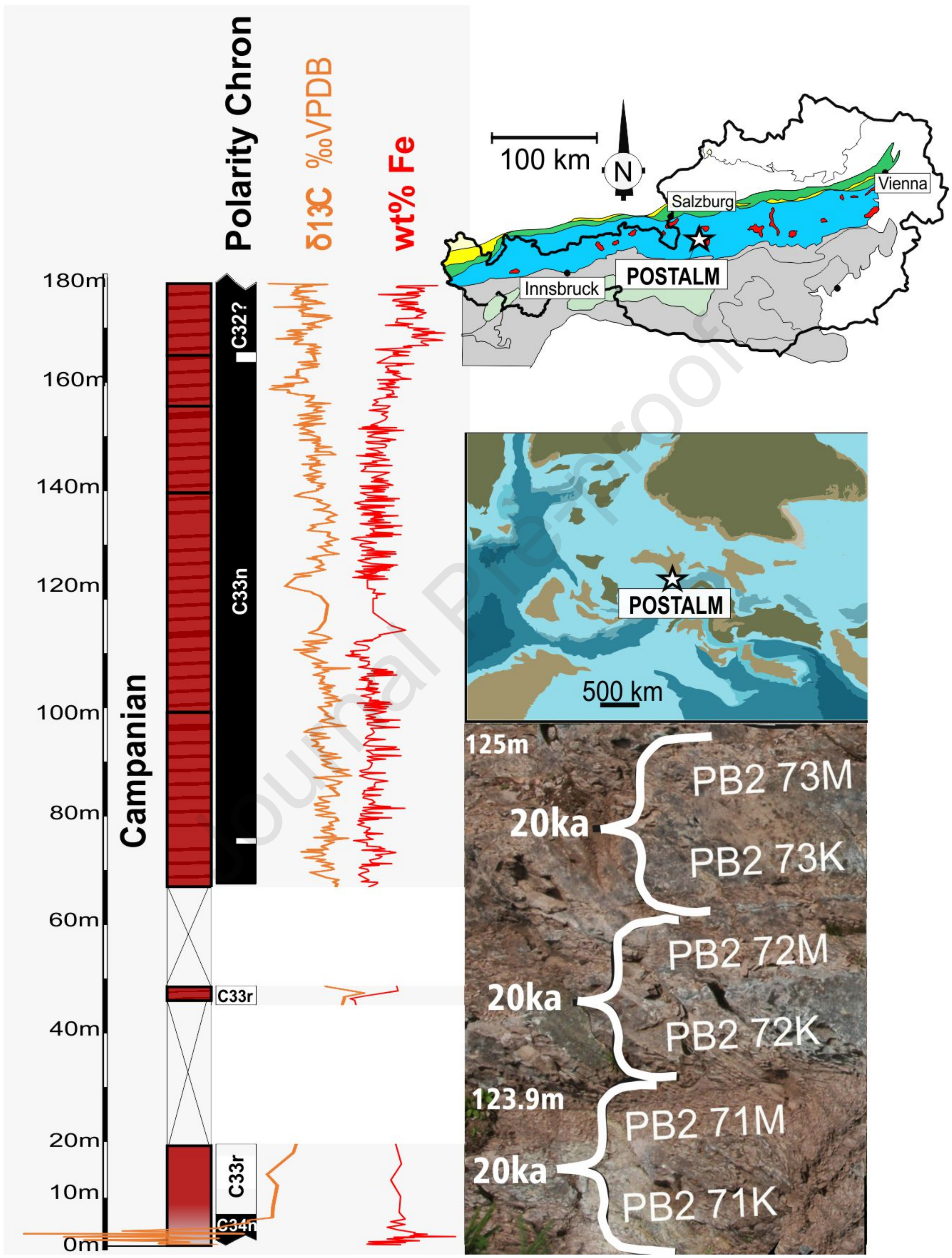
Polarity Chron
δ13C ‰VPDB
wt% Fe
180m
160m
140m
120m
100m
80m
60m
40m
20m
10m
0m
Campanian
C32?
C33n
C33r
C33r
C34n
100 km
N
Salzburg
Vienna
Innsbruck
POSTALM
POSTALM
500 km
125m
20ka
PB2 73M
PB2 73K
20ka
PB2 72M
PB2 72K
123.9m
20ka
PB2 71M
PB2 71K

An integrated multi-proxy study of cyclic pelagic deposits from the north-western Tethys: the Campanian of the Postalm section (Gosau Group, Austria)

Wolfgring, E.[1, 2], Wagreich, M.[1], Hohenegger, J.[3], Böhm, K.[4], Dinarès Turell, J.[5], Gier, S.[1], Sames, B.[1], Spötl, C. [6], Jin, S.D.[7]

[1]University of Vienna, Department of Geology, Althanstraße 14, 1090 Vienna, Austria

[2]Università degli Studi di Milano, Dipartimento di Scienze della Terra, Via Mangiagalli, 34, 20133 Milano, Italy

[3]University of Vienna, Department of Palaeontology, Althanstraße 14, 1090 Vienna, Austria

[4]Vrije Universiteit Amsterdam, Department of Earth Sciences, The Netherlands

[5]Instituto Nazionale di Geofisica e Vulcanologia, Vigna Murata 605, 00143 Rome, Italy

[6] University of Innsbruck, Institute of Geology, Innrain 52, 6020 Innsbruck, Austria

[7] Chengdu University of Technology, College of Energy Resources, Chengdu 610059, China

Abstract

The Upper Cretaceous Postalm section in the Northern Calcareous Alps (Austria) exposes pelagic deposits of the northwestern Tethys whose cyclostratigraphy and palaeoenvironments were examined in this study.

The section displays rhythmic deposits of Santonian to late Campanian age (Gosau Group). The Santonian/Campanian transition is characterised by condensed greyish carbonates, while the younger deposits are composed of reddish foraminiferal packstones displaying distinct limestone-marl alternations. A biostratigraphic framework based on planktonic foraminifera and calcareous nannofossils is supported by carbon and strontium isotope stratigraphy as well as magnetostratigraphy. The carbon isotope data allow to correlate the Postalm section to other Tethyan reference sites and to identify $\delta^{13}C$ events, such as the Late Campanian Event. Spectral analyses of three independently assessed proxies ($\delta^{13}C$, Fe content and the thickness of limestone/marl couplets) in the upper, continuously exposed section part identified 17 to 18 405 ka cycles spanning the mid to upper Campanian (*Contusotruncana plummerae* to *Gansserina gansseri* Zones or CC21/UC15c to CC23a/UC16 nannofossil zones).

Keywords: Campanian, cyclostratigraphy, magnetostratigraphy, foraminifera, nannofossils, stable isotopes

1. Introduction

The Campanian stage, first defined by Coquand (1857), and with an estimated duration of about 11.5 Ma (Gradstein et al., 2012), is the longest stage of the Late Cretaceous (Ogg et al., 2012) and was characterised by a significant change in the evolution of the climate system (Hay & Flögel, 2012). The Campanian, with a generally decreasing trend in global temperature levels, links the last offshoot of the mid-Cretacous super-greenhouse (hothouse) climate with its Oceanic Anoxic Events (i.e. OAE 3, Wagreich, 2012) to the onset of the Maastrichtian cooling (e.g., Jenkyns and Wilson, 1999; Pucéat et al., 2003; Hu et al, 2012; Linnert et al, 2014; Thibault et al., 2016; Huber et al., 2019).

To accurately constrain the timing and duration of processes affecting greenhouse climatic change in the Late Cretaceous, and the Santonian to Maastrichtian interval in particular, has been the focus of research in the past two decades, relying strongly on astrochronology (e.g., Herbert et al., 1995, 1999; Liu, 2007; Hennebert et al., 2009; Robaszkynski & Mzoughi, 2010; Voigt & Schönfeld, 2010; Husson et al., 2011; Thibault et al., 2012, 2016; Neuhuber et al., 2016; Wagreich et al., 2012; Batenburg et al., 2014, 2018; Wolfgring et al., 2017; Sinnesael et al., 2019). The “Astronomical Solutions for Earth’s Palaeoclimates” of Laskar et al. (2004, 2011) have become a reference to correlate cyclostratigraphic data and to harmonise floating timescales relying on astrocycles.

Researchers can choose from a variety of approaches to evaluate cyclostratigraphic data and astronomically tuned age models (see e.g., Strasser et al., 2006; Hinnov, 2012; Hilgen et al., 2015; Zeeden, et al., 2015; Sinnesael et al., 2019, etc). For this study, the lithological and physical characteristics of couplets in a rhythmite sequence (following the approach by Hohenegger et al. 2008; 2011, and Hohenegger and Wagreich 2012) and geochemical data were examined by spectral analysis.

This study aims at testing multiple cyclostratigraphic proxies from independent sample sets and analytical methods, (1) the physical parameters of limestone/marl couplets as measured in the field, (2) carbon isotopes measured by mass spectrometry, and (3) the concentration of Fe analysed by X-ray fluorescence (XRF). All three methods were used to establish and test an orbitally calibrated timescale for the mid to late Campanian. In a multistratigraphic framework, we present a Sr isotope record for the Campanian as well as magnetostratigraphic data correlated to planktonic foraminiferal and nannofossil biostratigraphic zonation that can be linked to a floating astronomical timescale. In addition, we also discuss carbon isotope events and their validity for global correlation in the Late Cretaceous fading greenhouse.

2. Geological setting

Sedimentary rocks included in the thrust units of the Northern Calcareous Alps (NCA) were originally deposited along the northern margin of the Austroalpine domain on the Adriatic microplate (Wagreich, 1993). Situated along the southern margin of the Penninic Ocean ("Alpine Tethys" of Stampfli & Borel, 2002; Handy et al., 2010), which was a north-western branch of the Tethys oceanic system (see also Neuhuber et al., 2007), the NCA represent an active plate margin (Fig. 1).

In the NCA, the Upper Cretaceous to Paleogene Gosau Group comprises deposits of the terrestrial to shallow marine Lower Gosau Subgroup and the deep-water deposits of the Upper Gosau Subgroup. The Lower Gosau Subgroup of Turonian to Santonian age filled pull-apart basins alongside an oblique subduction — strike-slip zone (Wagreich & Decker, 2001). After a short phase of tectonically induced uplift, rapid subsidence resulted in the sedimentation of the pelagic, hemipelagic and turbiditic Upper Gosau Subgroup (Wagreich, 1993; Krenmayr, 1999; Wagreich et al., 2011; Hofer et al., 2011). The Santonian to Eocene Upper Gosau Subgroup and the underlying Lower Gosau Subgroup are separated by an angular unconformity (Wagreich and Krenmayr, 2005).

#################### Fig1

The southern, active continental margin of the Penninic Ocean (Wagreich, 1993) exhibited a rather restricted environment with minor connections to the open Tethys ocean during the mid-Cretaceous (e.g. Gebhardt et al., 2010), while a well-connected "open Tethyan" palaeoceanographic setting was reconstructed for the Late Cretaceous (Wagreich et al., 2012; Wolfgring and Wagreich, 2016). Figure 1 shows the palaeogeographic setting and the location of the studied area during Late Cretaceous times.

The neritic to pelagic deposits of the Nierental and Bibereck Formations of the NCA are part of the Upper Gosau Subgroup and were deposited in a low to mid-latitude setting at approximately 30 to 35°N paleolatitude (Krenmayr, 1996; Wagreich & Krenmayr, 2005;

Wagreich et al., 2012). The distinctly reddish Nierental Formation overlies the grey coloured Bibereck Formation which records the development from an inner neritic shelf environment to an outer neritic to upper slope environment; this deepening trend continues upsection into the Nierental Formation (Wagreich and Neuhuber, 2005; Wagreich and Krenmayr, 2005; Wolfgring et al., 2016; Wolfgring and Wagreich, 2016).

The Postalm section (WGS84 coordinates 13°23′11″E, 47°36′44″N) covers the upper Santonian Bibereck- and the Santonian to Maastrichtian Nierental Formation and was part of a northward deepening slope. Rhythmites displaying distinct marly limestone — marl cycles (Fig. 2) are restricted to the Nierental Formation (Wagreich et al. 2012). These marly limestones can be classified as foraminiferal packstone and record a pelagic depositional environment well above the carbonate compensation depth (CCD). They have been interpreted as Cretaceous Oceanic Red Beds (CORB), documenting well oxygenated bottom waters (Hu et al., 2005; Wagreich & Krenmayr, 2005). A detailed mineralogical and sedimentological assessment is available in Neuhuber et al., 2016.

#################fig2

3. Material and Methods

3.1. Sampling and field measurements

Over 550 rock samples were collected within the ~178 m thick Postalm section. Aiming at a “per cycle” resolution, sampling for biostratigraphic and geochemical analyses was performed bed by bed. An additional 144 samples were collected for magnetostratigraphy (“Pm” samples) and 16 for Sr isotope analysis (“Po” samples).

5 subsections were logged at the Postalm section (subsections A to E, see Fig. 3), as faults and exposure gaps suggested a discontinuous record and field observations pointed to changes in the sedimentation rate. The average sediment accumulation rate was estimated to 19 mm/ka (Wagreich et al. 2012) for subsections A to D. Increased siliciclastic

sediment input in the uppermost parts of the section is recorded by frequent thin (< 5 cm in thickness) turbidite beds (in subsection E). Detailed drawings of subsections A to E as well as exemplary micrographs of thin sections are provided in the supplementary material (Appendix 1-7). For more detailed information on the geological setting of the Postalm section the reader is referred to Wagreich et al. (2012) and Neuhuber et al. (2016).

###########fig 3

3.2. Palaeomagnetic sampling and methods

The palaeomagnetic sampling was mostly carried out using a portable rock core drill although oriented hand-samples were also taken in the studied section. All samples were oriented in situ with a magnetic compass and standard cubic or cylindrical specimens were subsequently cut in the laboratory for paleomagnetic analysis. A total of 144 stratigraphic horizons were sampled along the 178 m long studied section with an average resolution of 0.9 m (two sampling gaps of about 20 m and 30 m exist in the lower third of the section due to covered outcrop).

Natural remanent magnetization (NRM) and remanence through demagnetization were measured on a 2G Enterprises DC SQUID high-resolution pass-through cryogenic magnetometer (manufacturer noise level of 10-12 Am^2) operated in a shielded room at the Istituto Nazionale di Geofisica e Vulcanologia in Rome, Italy. A Pyrox oven in the shielded room was used for thermal demagnetizations and alternating field (AF) demagnetization was performed with three orthogonal coils installed inline with the cryogenic magnetometer. Progressive stepwise AF demagnetization was routinely used and applied after a single heating step to 150℃. AF demagnetiz ation included 14 steps (4, 8, 13, 17, 21, 25, 30, 35, 40, 45, 50, 60, 80, 100 mT). Stepwise full thermal demagnetization was performed in some sister specimens up to 600℃. Cha racteristic remanent magnetizations (ChRM) were computed by least-squares fitting (Kirschvink, 1980) on the orthogonal demagnetization plots (Zijderveld, 1967). The latitude of the virtual geomagnetic pole (VGP) of each sample is used to define magnetic polarity. The method that calculates VGP latitude relative to the sampling site was employed (i.e Lowrie et al., 1980). The method first derives the site latitude at the time of deposition from the mean ChRM inclination data which is then used with the individual ChRM declination and inclination for each sample to compute the instantaneous relative VGP latitude. This parameter was taken as an indicator of the original magnetic polarity, normal polarity being indicated by positive VGP latitudes and reverse polarity by negative VGP latitudes (Fig. 4).

################Fig 4

3.3. Biostratigraphy

Planktonic foraminifera and calcareous nannoplankton was used to establish a robust biostratigraphic framework. Samples including those for scanning electron microscopy (SEM) as well as microslides are stored in the Earth Science collections at the Department of Geodynamics and Sedimentology, University of Vienna. SEM images were taken with a JEOL JSM 6400F operating at 10 kV at the Department of Palaeontology at the University of Vienna.

3.3.1. Planktonic foraminiferal biostratigraphy

Foraminiferal biostratigraphy was assessed using 221 marl and marly-limestone samples. Samples were disaggregated with the tenside Rewoquad© and, if a considerable amount of organic matter was present, were soaked overnight in hydrogen peroxide. After washing through 4 mm, 125μm and 63μm sieves, the samples were dried overnight at 50℃. The >125μm fraction was used exclusively for qualitative biostratigraphic investigations. The overall state of preservation of planktonic foraminifera was moderate to poor. Samples were scanned for the presence of biostratigraphically indicative taxa. Planktonic foraminiferal taxonomy follows Nederbragt (1991), Robaszynski and Caron (1995) and Premoli Silva and Verga (2004), and the suprageneric classification is according to Loeblich and Tappan (1988).

3.3.2. Calcareous nannoplankton biostratigraphy

149 smear slides were prepared for calcareous nannofossil investigations using scratched sediment powder suspended with distilled water in a beaker. After 2 hours, the superfluent containing mainly clay-size particles was discarded, the sample was prepared by

resuspending the settled material from which droplets were put on a glass cover plate, air dried, and then fixed with Canada balsam on a glass slide. These slides were examined qualitatively using a polarized-light microscope for marker species and nannofossil biostratigraphy. Taxonomy follows Burnett (1998) and the Nannotax 3 online resource (Young et al., 2017; www.mikrotax.org/Nannotax3/).

3.4. Geochemistry

3.4.1. Stable carbon and oxygen isotope stratigraphy

Carbon and oxygen isotopes of 438 rock samples were measured using a ThermoFisher Delta^{puls}XL isotope ratio mass spectrometer equipped with a GasBench II at the Institute of Geology (University of Innsbruck), following the procedure described in Spötl and Vennemann (2003). The results were calibrated against NBS 19, CO1, and CO8 standard reference materials and are reported on the VPDB scale (see Fig. 3 and table A1 in supplementary materials).

3.4.2. Sr isotope stratigraphy

Sr isotopes were analysed in the Laboratory of Geochronology at the Department of Lithospheric Research, University of Vienna. Samples were leached in different concentrations of CH_3COOH and element separation followed conventional procedures, using an AG 50 W-X8 (200e400 mesh, Bio-Rad) resin and HCl as elution medium.

Sr fractions were loaded as chlorides and vaporised from a Re double filament in a ThermoFinnigan Triton TI thermal ionisation mass spectrometer. Total procedural blanks for Sr were 1 ng. A $^{87}Sr/^{86}Sr$ ratio of 0.710249 ±0.000004 was determined for the NBS987 international Sr standard during different runs, and ratios were recalculated according to a NIST 987 value of 0.710248 (McArthur et al., 2001). Within-run mass fractionation was corrected for an $^{86}Sr/^{88}Sr$ value of 0.1194. Analytical errors are reported as ±2s standard deviation (see also Wagreich et al., 2012).

3.4.3. Fe chemostratigraphy

517 pulverized rock samples were scanned by a handheld XRF device acquiring bulk sediment data (Bruker Tracer IV SD handheld XRF analyser with a 10 mm² X-flash silicon drift detector) (Fig. 4 and, for calibrations, table A2 in the supplementary materilals). Internal standards based on ICP-MS data of rock powders were used to calibrate the device (see table A2 in the appendix for a detailed list of samples). Repeated

measurements of the Fe content yielded a standard deviation of 0.12%.

3.5. Orbital cyclicity and astronomic calibration

We use geochemical data (carbon isotopes and the Fe content) as well as data from the lithostratigraphic assessment of the Postalm section (profile segments B1, B2, C, D, and E; 66m – 178m) to examine harmonic frequencies in the dataset and establish a cyclostratigraphic model.

The power spectral method described in Hohenegger et al. (2008) and Hohenegger and Wagreich (2012) was applied to detect rhythmic frequencies preserved in limestone/marl thickness data. We calculated a standardised thickness for limestone-marl couplets that are believed to represent precessional signals (see Herbert et al., 1999; Wagreich et al., 2012; Eldrett et al., 2015). In the following, limestone/marl data are treated as “per-cycle” data with an average duration of 19-20 ka per couplet.

Note that the calculation of orbital signals recorded in the $\delta^{13}C$ signal or the Fe content does not use the standardised thickness of limestone/marl couplets (and the duration of precession cycles), but relies on fitting the duration of the prominent 405 ka cycle to an average sedimentation rate. An average sedimentation rate of 1.9 cm/ ka was applied to transform the harmonic frequencies preserved in the $\delta^{13}C$ and Fe records to the time domain (see Wagreich et al., 2012; Neuhuber et al., 2016; Wolfgring et al., 2016, 2018).

The programme packages PAST (Hammer and Harper, 2006), R (R Core team, 2016) with the software packages “dplR” (Bunn, 2010, Bunn et al., 2015) and “astrochron” (Meyers, 2012; 2014) were applied. Spectral peaks were calculated using Redfit (Schulz and Mudelsee, 2001; Thomson, 1982) and Evolutive Harmonic Analysis (EHA; Meyers, 2014; Thomson, 1982). Spectral analyses were performed separately on the older and younger parts of the section separately as a gap at 124 m (mid B2). The two segments represent data from 62 m (base B1) to 120 m and from 120 m to the top of the Postalm section at 178 m (top PE).

Before calculating spectral density, mean values and linear trend were removed (see “astrochron” documentation, Meyers, 2014). If required, data were interpolated using piecewise linear interpolation. The Redfit analysis used in this paper implements a Monte Carlo simulation (500 simulations) and a rectangular window was used for scaling the data. An oversampling factor of 2 and 21 AR1 simulations were used in the calculations.

EHA was calculated separately for every proxy and for both subsections, 66.17m to

118.52m and 120 to 178.12m (B1-B2a and B2b to E). EHA of $\delta^{13}C$ and Fe used a moving window of 800 cm with steps of 40 cm and a time bandwidth product (tbw) of 3. For the L/M series a window of 40 cm and a step of about 2 couplets (~100cm) and a tbw of 3 were applied. Changes in the sedimentation rate were assessed following the spectral drift of the 405 ka cycle that is visualised in the EHA. Data were subsequently tuned to the spectral signal of the 405 ka cycle, to account for changes in sedimentation rates. The margins of the tuned time series were extrapolated applying the determined sedimentation rates (for detailed information see the “astrochron” documentation, Meyers, 2014).

Significant orbital frequencies were isolated using a bandpass filter with a rectangular window. Signals were band-passed to wavelengths corresponding to the 405 ka and 100 ka eccentricity signals. In an attempt to synchronise Fe and $\delta^{13}C$ data, the bandpass filter was designed to match both the 405 ka signal in the Fe and the $\delta^{13}C$ data.

To extract the 405 ka signal in the lower parts of the Postalm section (B1-B2a) the bandpass filter used in L/M alternations centred on 20.5 precession cycles (16-25 couplets). Bandpass filters used for the Fe and $\delta^{13}C$ data were centred on a frequency of 0.00125 (800 cm, frequency band 0.0015-0.001) for the 405 ka cycle. To extract the 405 ka signal in the upper parts of the outcrop (120m -178,12m), the bandpass filter used in L/M alternations was centred on 20 precession cycles (14 to 25 couplets); filters used for Fe and $\delta^{13}C$ data were centred on a frequency of 0.0013 (769.23 cm, frequency band 0.0009-0.0022).

To extract the 100 ka signal in the lower segment , from 66.17m - 118.52m (B1-B2a), the bandpass filter used in L/M alternations was centred on 5.1 precession cycles (frequency band 0.25-0.16 or 4-6.2 couplets) and in the overlying segment from 120m - 178.12m (B2-E). a bandpass filter centred on 5 precession cycles (frequency band 0.25-0.165 or 4-6 couplets) was applied.

To extract the 100 ka signal in older strata (66.17m -118.52m), the bandpass filters used for Fe and $\delta^{13}C$ data were centred at a frequency of 0.00415 (240.9 cm) and a frequency of 0.005 (200 cm) for the 100 ka signal in the younger deposits (120m – 178.12m, segments B2b-E).

In an attempt to match data obtained in this study to the Laskar solution and the cyclostratigraphic solution for the Maastrichtian (Laskar et al., 2004, 2011; Husson et al., 2011) the two profile segments were correlated using bio- and magnetostratigraphic properties and statistical means. A tapered cosine window was applied to bandpass the Laskar solution, and the tuned carbon isotope and Fe timeseries to the 405 ka and 100 ka signals (centred at a frequency of 0.00247 for 405 ka and 0.01 for 100 ka). The base of the older profile segment of the Postalm section is constrained by the base of magnetochron C33n (at approximately 79.9 Ma, Ogg, 2012). In the upper 120 – 178.12m (B2b to E), we use the top of the *R. calcarata* Zone and the top of magnetochron C32r.1r as constraints. Two options for astrochronologically calibrated datums for the top of the *R. calcarata* Zone and magnetochron C32r.1r are given in Husson et al. (2011). Figures, durations and correlations published in this study rely on ages published in the cyclostratigraphic models and correlations of Husson et al. (2011) and Thibault et al. (2012). We use an age of 73.19 Ma (73.6 Ma in option 1 of Husson et al., 2011) for the top of C32r.1r and 74.7 Ma for the top of the *R. calcarata* biozone (75.1 Ma in option 2).

4. Results

4.1. Palaeomagnetic results and magnetostratigraphy

The NRM intensity of the studied specimens generally ranges from 3 x10^{-3} to 25 x10^{-3} A/m, with reverse samples having lower values around 1 x10^{-3} A/m due to overlap of a secondary component. The intensity of the samples dropped noticeably after the first heating step at 150℃ and proceeded up to about 17- 21 mT (or up to 250-300℃), demagnetising a secondary viscous component (see Fig. 4).
Above these demagnetizing fields, up to about 80-100mT (or up to 600-640℃), demagnetization trajectories trending toward the origin defined the characteristic remanent magnetization (ChRM). The ChRM components present dual polarity in tilt-corrected coordinates suggesting a primary origin for this component (supplementary material Fig. A7). The combined thermal and AF demagnetization suggests that the magnetic carrier is dominated by a low-coercivity mineral (likely magnetite) together with some contribution of a high-coercivity mineral than unblocks above 580℃ (likely hematite). Wolfgring et al.

(2018) documented isothermal remanent acquisition (IRM) experiments and thermomagnetic curves from 0 to 17.01m (section PA).

The derived VGP latitude (Fig. A8 in supplementary materials) defines a lower normal polarity interval (1.9-2.5 m) and a reverse interval in the upper part (4-7 m). A detailed study of the Santonian-Campanian transition at the Postalm section was presented in Wolfgring et al., 2018). The C34n/C33r boundary was pinpointed within a 15 cm interval from 2.66 to 2.81 m.

A single but high-quality reverse sample is present at 165.12 m (PT89A) embraced by normal polarity samples at 162.82 m and 166.10 m, respectively. As sample PM89 occurs just above a fault between subsections D and E, it is suggested that the top of chron C32r.1r could be delineated in the interval 165.12-166.10 m in section E. Chron C32r.1r has an astronomically calibrated duration of 0.3 [±0.06] Ma (Husson et al, 2011) and could have been partially truncated by the aforementioned fault.

4.2. Planktonic foraminiferal biostratigraphy

The planktonic foraminiferal zonation in this study follows the Tethyan standard zonation of Premoli Silva and Sliter (1995), modified by Petrizzo et al. (2011). The detailed biostratigraphy of the Santonian-Campanian transition was already published in Wolfgring et al. (2018). Seven planktonic foraminifera zones were identified, ranging from the uppermost Santonian *Dicarinella asymetrica* Zone, the lower Campanian *Globotruncanita elevata* Zone, the *Contusotruncana plummerae* Zone, the *Radotruncana calcarata* Zone, the *Globotruncanella havanensis* Zone, the *Globotruncana aegyptiaca* Zone to the Campanian to early Maastrichtian *Gansserina gansseri* Zone. Biostratigraphic ranges of marker taxa are illustrated in Fig. 5, and SEM micrographs of some stratigraphically indicative species are depicted in Fig. 6.

############# fig 5

############# fig 6

4.2.1. *Dicarinella asymetrica* Zone

This zone comprises the total range of the nominative taxon. The highest occurrence (HO) of *D. asymetrica* was at 4.05 m (sample PA20) and *Muricohedbergella flandrini* at 3.45 m (sample PA19). *Globotruncanita elevata* is continuously present in this section (Wolfgring et al., 2018). *Marginotruncana coronata*, *M. marginata* and *M. pseudolinneiana* are common elements, but marginotruncanids show an overall decline in numbers. Abundant double keeled globotruncanids (*G. linneiana, G. neotricarinata, G. bulloides, G. falsostuarti*) and single keeled *Globotruncanita stuartiformis* were identified. Bi- and multiserial foraminifera identified in this zone include *Pseudotextularia nuttallii* and *Ventilabrella eggeri.* We did not identify the Santonian marker taxon *Sigalia* spp.

4.2.2. *Globotruncanita elevata* Zone

The interval from the HO of *Dicarinella asymetrica* to the lowest occurrence (LO) of *Contusotruncana plummerae* is defined as the *Globotruncanita elevata* Zone. The nominative taxon shows a consistent appearance throughout this zone. *Contusotruncana fornicata, C. patelliformis* and *C. morozovae* are very abundant. The first biconvex double keeled morphotype that can clearly be attributed to *Globotruncana arca* appears at the base of this zone. The abundance patterns of other double keeled globotruncanids show no significant changes upsection compared to the *Dicarinella asymetrica* Zone. The HO of *Globotruncanita atlantica* is evident at 45.6 m (sample PX1). *Globotruncanita stuartiformis* is very abundant. Marginotruncanids are still present but show a discontinuous record. Bi- and multiserial planktonic foraminifera are exceedingly rare. Ventilabrellids disappear at the base of *G. elevata* Zone.

4.2.3. *Contusotruncana plummerae* Zone

This zone is defined by the interval between the LO of *Contusotruncana plummerae* and the LO of *Radotruncana calcarata.* It was established to replace the *Globotruncana ventricosa* Zone (Petrizzo et al., 2011).

Contusotruncana sp. aff *C.plummerae* is recorded from PX1. The specimens exhibit three to four chambers in the last whorl and laterally inflated chambers, as well as two keels that display an oblique offset. The LO of *Contusotruncana plummerae* is recorded at 73,5 m (sample PB1/21M), the LO of *Globotruncana ventricosa* at 84.4m (in samplePB1/59M) . The HO of *Globotruncanita atlantica* occurs at 130.48 m sample PB2/86M. The HO of marginotruncanid taxa is also recorded in this zone (*M. coronata* in subsection B2). *Globotruncana* spp. and *Contusotruncana* spp. dominate this interval. Large biserial forms are very rare and predominantly represented by *Pseudotextularia nuttallii*. Rugoglobigerinids (*Rugoglobigerina rugosa, R.* sp. cf. *R. macrocephala*) are present in this interval and appear in small morphotypes showing a discontinuous record. The LO of *Rugoglobigerina rugosa* is at 124 m, while the LO of *Radotruncana subspinosa* is recorded at 136 m (PB2/107M), 3.6m below the LO of *R. calcarata*.

4.2.4. *Radotruncana calcarata* Zone

This zone is defined by the total range of the index species. The LO of *Radotruncana calcarata* was recorded at 139.6 m (in sample PB2/34M). The *Radotruncana calcarata* Zone recorded at the Postalm section was a stable planktonic foraminiferal community that showed remarkable continuity and similarity to the stratigraphically older sequences in this section. Apart from the sudden appearance and disappearance of the zonal marker, the HO of *Globotruncanita elevata* occurs at 142 m (PC8/1) and the LO of *Gublerina rajagopalani* at 134 m (sample PC7/40). *Globotruncanella havanensis* is a rare new element and occurs at 140.7 m (PC7/36) and 150 m (PC8/04) in this zone. *Contusotruncana* sp. cf. *C. plicata* was identified at 152.25 m (in sample PC8/5B) and shows a discontinuous record upsection. *Globotruncanella pschadae* and *Gl. petaloidea* first appear during the *R. calcarata* interval. The microstratigraphy of this particular interval was investigated in Wagreich et al. (2012), Wolfgring et al. (2016), Wolfgring and Wagreich (2016).

4.2.5. *Globotruncanella havanensis* Zone

This interval covers the time from the HO of *Radotruncana calcarata* (at Postalm section coinciding with the HO of *R. subspinosa*) at 155.6 m (sample PC09-08/10M) to the LO of *Globotruncana aegyptiaca* at 162.6 m in sample PD23K. We observed an increase in the abundance of rugoglobigerinids in this zone. The taxon *Rugoglobigerina hexacamerata* has its LO at 162.6 m (sample PD23K). *Globotruncana dupeublei* appears as rare element at the base of the *havanensis* Zone (at 155 m). The amount of biserial planktonic foraminifera increases in this zone, but double keeled globotruncanids constitute still the dominant faunal element.

4.2.6. *Globotruncana aegyptiaca* Zone

This zone defines the interval from the LO of the index species (162.6 m, PD 23K) to the LO of the planktonic foraminifer *Gansserina gansseri* (171.5 m, PE 26T). The LO of

Pseudoguembelina excolata was recorded at 162.4 m, in PD23K. We also observed the LO of *Praegublerina pseudotessera* in this sample. We identified the LO of several taxa in this interval. The composition of the planktonic foraminiferal assemblage changes significantly within this zone. Rugoglobigerinids, biserial forms as well as diverse globotruncanellids become very abundant and show a general increase in size. The LO of *Rugoglobigerina macrocephala* occurs at at 166.2 m (PE6), *R. pennyi* at 167.1m (PE9) and *R. milamensis* at 168.4 m (in sample PE14). *Gansserina* sp. *G.* cf. *wiedenmayeri* is recorded at 166.2 m (PE6) for the first time, as well as *Contusotruncana walfischensis* at167.1 m (P9). The multiserial form *Planoglobulina* sp. *P.* cf. *carseyae* shows its LO at 167.9 m, PE11. The same sample shows the LO of *Gublerina acuta*. The LO of *Globotruncanita conica* was found in the topmost parts of the *Globotruncana aegyptiaca* Zone (169.3 m, PE19).

4.2.7. *Gansserina gansseri* Zone

The late Campanian to early Maastrichtian *Gansserina gansseri* Zone defines the interval from the LO of *G. gansseri* to the LO of *Abatomphalus mayaroensis.* The LO of *G. gansseri* was observed in sample 171m (PE26T). This zone covers the topmost strata of the outcrop. Neither *Abatomphalus mayaroensis* nor *Contusotruncana contusa* were identified. The index species *Gansserina gansseri* is extremely rare, and this zone is characterised by the high abundance of *Globotruncanella* spp. (*G. havanensis, G. pschadae, G. petaloidea*) and *Rugoglobigerina* spp. The LO of *Racemiguembelina* ? *powelli* was identified as the highest bioevent at 177.9m (PE46).

4.3. Calcareous nannoplankton biostratigraphy

Nannofossil samples typically show poor to moderate preservation, with moderate to strong overgrowths up to the point where in some diagenetically altered samples species and genus determination was not possible. Nannofossil abundance varies considerably between 0.5 to 30 nannofossils per field of view.

The biostratigraphic zonation at the Postalm section follows the UC zonation (TP-“tethyan-intermediate”) of Burnett (1998) and the Sissingh (1978) and Perch-Nielsen (1985) nannofossil standard zones (CC-Zones). The ranges of stratigraphically significant nannofossil taxa are depicted in Figure 7, some calcareous nannofossil marker taxa are illustrated in Figure 8.

################fig 7

################fig 8

4.3.1 Nannofossil zone UC13

The base of the Postalm section, (0- 17.01m), comprises nannofossil zone UC13, defined by the first (and sporadic) occurrence of *Arkhangelskiella cymbiformis*. Some other marker species include *Marthasterites furcatus, Amphizygus brooksi, Calculites obscurus, Eiffellithus eximius, Lithastrinus grillii, Lucianorhabdus cayeuxii* (including curved morphotypes, *L. cayeuxii* B sensu Wagreich 1992), *Micula staurophora, Reinhardtites anthophorus.* This interval from 0 to 4.47 m correlates with zone CC17 of Perch-Nielsen (1985) and the CC17b subzone of Wagreich (1992).

4.3.2 Nannofossil zone UC14a

The base of UC14a was defined by the LO of *Broinsonia parca parca* (large morphotype > 9 µm, and a central area to shield ratio below 2, see Wolfgring et al., 2018) at 4.47 m. In addition, *Ceratolithoides* cf. *verbeekii* has its sporadic LO within this interval.

[4.47 – 20 m]

4.3.3 Nannofossil zone UC14b (UC14b-c-d - UC15a]

The base of UC14b and CC18b of Perch-Nielsen (1985) was defined by the LO of *Broinsonia parca constricta* (large morphotype > 9 µm, and a central area to shield ratio below 1, see Wolfgring et al., 2018). This interval starts at 20 m, below a covered interval that includes probably subzones UC14b, UC14c, UC14d and UC15a which could not be detected at Postalm.

[20-21m]

4.3.4. Nannofossil zone UC15b

The LO of *Ceratolithoides aculeus* defines the base of UC15b (Burnett, 1998) and CC20 (Perch-Nielsen, 1985). Due to the poor outcrop quality within this middle part of the Postalm section the LO of the marker species is at ca 47 m (sample PX-PM139). The HO of *Lithastrinus grillii* occurs also within this zone at 80.24 m (PB1/47M), and the HO of the

very rare *Lucianorhabdus maleformis* at 94.52 m (PB1/87K).
[47.00-112.25m]

4.3.5. Nannofossil zone UC15c

Zone UC15c (Burnett, 1998) is defined by the LO of *Uniplanarius sissinghii*, corresponding to CC21 (Perch-Nielsen, 1985). *U. sissinghii* occurs at 112.26 m (PB2/48M). Within this zone, several secondary nannofossil markers have their sporadic LO such as *Lithraphidites praequadratus* and *Eiffellithus gorkae*.
[112.26-137.37m]

4.3.6 Nannofossil zone UC15d-e

The LO of *Uniplanarius trifidus* defines the base of UC15d and CC22 at 137.53 m (PB2/110K), just below the LO of *Radotruncana calcarata* (see also Wagreich et al., 2012). *Eiffellithus eximius* is rare and could not be found in all samples but is still present throughout this interval.
[137.53-162.21m]

4.3.7 Nannofossil zone UC16

The base of UC16 (and CC23a of Perch-Nielsen, 1985) was defined by the HO of *Eiffellithus eximius* at 162.21 m (PD/23K). The secondary marker, the HO of *Reinhardtites anthophorus*, was recorded at 163.42 m (PD/27M). *Broinsonia parca constricta*, defining the base of UC17 and CC23b by its HO (Perch-Nielsen, 1985) just below the base of the Maastrichtian (Burnett, 1998), is present up to the top of the Postalm section (PE/48T), indicating UC16 up to the end of the section. Also, *Uniplanarius trifidus* and *Tranolithus orionatus* are still present up to the topmost sample of the section at 178.12 m.

4.4. Age-depth model

We compared the top of magnetochrons C34n (83.64 Ma, according to Ogg and Hinnov, 2012) and C32r.1r (73.19 Ma, according to option 1 presented in Husson et al. ,2011) as well as nannofossil and foraminiferal event datums to the age model of Coccioni and Premoli Silva (2016) from the Gubbio section (Italy) (Fig. 9 and Tab. 1). The Bottaccione and Contessa sections were chosen due to their palaeogeographical proximity in the western Tethys and similarity in their depositional environment to the Postalm section. The paleolatitude of the Gubbio section was 30°N during the Late Cretaceous and these reddish rhythmite sequences referred to as CORBs were deposited in a pelagic setting (Sliter and Premoli Silva, 1995; Coccioni and Premoli Silva, 2016). Where relevant data from the Gubbio section are unavailable, datums of bioevents in the age-depth model refer to Scott (2014). The age-depth model (Fig. 9) shows a linear fit (R^2=0.9) to the nannofossil and planktonic foraminiferal ages of Coccioni and Premoli Silva (2016) and Scott (2014). Datums of Scott (2014) were used exclusively for the LOs of *Arkhangelskiella cymbiformis* and *Ceratolithoides verbeekii* and the HO of *Eiffelithus eximius*. Discrepancies in the age model are evident in the LO of *Ceratolithoides verbeeki*, the FO of *Globotruncana atlantica* as well as the HO *Eiffelithus eximius* (Fig. 8). The LO of *Planoglobulina carseyae* is based on a fragmented specimen recovered at the Postalm section.

####################fig9

##################table 1

4.5. Isotope chemostratigraphy

4.4.1. Carbon isotope stratigraphy

The composite carbon isotope curve covers ~178 m. $\delta^{13}C$ values from the base of the Postalm section to ~4 m (covering the initial part of the section, the Santonian-Campanian boundary interval) show fluctuations from 0 to 1.9 ‰. The subsequent values fluctuate with low amplitudes between 1.9 and 2.5‰ (Fig. 5). A significant negative excursion of >-0.5‰ is evident between 150 and 160 m. This excursion could be related to the Late Campanian Event (LCE, Jarvis et al., 2002; Wendler, 2013). Figure 10 shows possible correlations of the Postalm carbon isotope curve to other sections.

Apart from the strong fluctuations recorded in the oldest deposits of this section we identified a steady decrease in $\delta^{13}C$ between 45 and 178.12 m from 2.5 to 2.2 ‰. The $\delta^{13}C$ values between 66.44 and 178.12 m fluctuate around the mean of 2.31‰ with a standard deviation of 0.12‰. Two negative excursions are present at 120 m (corresponding to a minor discontinuity in segment B2) and at 159 m (no visible change in the lithology).

####################figure 10

4.5.2. Oxygen isotope data

Oxygen isotope values are weakly correlated with the carbon isotope values (r=0.32) and show negative values of -4‰ close to the Santonian-Campanian boundary (see supplementary material). This is followed by an increase to around -1‰ up to ~17 m . From segment X to the top of the section the $\delta^{18}O$ values remain rather invariant with a mean of $\delta^{18}O$ at -1.4 ± 0.6‰.

Wolfgring et al. (2018) identified a significant diagenetic overprint of the stable isotope composition at the base of the Postalm section, 0-~17 m (subsection A), where the $\delta^{18}O$ values are significantly positive correlated with the $\delta^{13}C$ values, and the correlation between oxygen and carbon isotopes for the entire section is consistent with this interpretation (despite a weaker correlation in the younger parts of the section). Therefore, we refrain from using the oxygen isotopes for cyclostratigraphy and palaeoenvironmental interpretations.

4.5.3. Strontium isotope stratigraphy

The sixteen Sr isotope analyses show a steady increase in the $^{87}Sr/^{86}Sr$ ratio from 0.707531 ±0.000003, $^{87}Sr/^{86}Sr$-sample Po17 at sample PA 11 (1.3 m) to 0.707758 ±0.000004 at the top of the section (sample Po1 at 178.2 m, see Fig. 11). $^{87}Sr/^{86}Sr$ values show a continuous increase up to the top of segment B2 and values follow roughly a continuous linear trend as expected for the Late Cretaceous (McArthur et al., 1994, 2001). Samples Po7 and Po6 show a drop to 0.707649 ±0.000006, followed by a pronounced increase in Po5 (0.707759 ±0.000005). The topmost three samples define a decline of the curve in Po4 (0.707720 ±0.000004), a small increase in Po3 (0.707768 ±0.000006) and finally a slight drop in Po1 (0.707758 ±0.000004). For comparison, the $^{87}Sr/^{86}Sr$ composite reference curve for the Campanian of McArthur et al. (2012) is plotted in grey (Fig. 11).

#####################figure 11

4.6. Fe content

The values of Fe vary between 1.5 and 3 wt% and increase to 5 wt% towards the upper part of the Postalm section (165 - 178.12 m, section PE, Fig. 4). Fe is negatively correlated with $\delta^{13}C$ (r = -0.30).

4.7. Spectral analysis

Figure 12 shows the results of Redfit spectral analyses from combined L/M couplets as well as for the Fe and $\delta^{13}C$ data and the EHA results are given in Figure 13.

4.7.1. Redfit analyses

Redfit analyses were calculated for the three datasets (L/M, $\delta^{13}C$ and Fe) for two profile sections: 120.02-178.12 m (B1- B2a), 66.44-118.52m (B2a to E, see Figs. 12a, b, c).

Most analyses show a signal exceeding the 99% confidence interval (CI) that could be related to a 405 ka harmonic that supposedly represents the most stable astronomical cycle in the Mesozoic (Berger et al., 1992; Laskar et al., 2011. A relevant signal at 8.5 m (466 ka) is masked in the $\delta^{13}C$ spectrum between 66.44 - 182.52 m (B1-B2a) by a 17 m cycle that corresponds to a duration of 933 ka. This signal is of unclear harmonic origin and could possibly be explained by stacked harmonic frequencies in the eccentricity band. The Fe record shows the highest sampling density and therefore the highest spectral resolution. On the contrary, the L/M record shows the least number of data points and the lowest spectral resolution.

The L/M record follows a per-precession cycle log. The maximum spectral resolution is, considering the Nyquist frequency, in the frequency band of obliquity cycles (at approximately 40 ka - Weedon, 2003). We found signals of a 494 ka cycle in the older profile segment (66.44-118.52 m, B1-B2a) and of a 404 ka cycle in the younger part of the section (120.02 – 178.12 m, B2b-E). The L/M record shows clear 100 ka eccentricity harmonics. Peaks of 4.7 precession cycles (89 ka) at 66.44-118.52 m (B1-B2a) and of 5.3 cycles (98 ka) at 120.02 – 178.12 m (B2b-E) exceed the 99% CI. We furthermore find evidence of obliquity terms in the two segments of the Postalm section. Signals with periods of 2.5 (47 ka) and 2 precession cycles (39 ka) in the older segment (66.44 – 118.52m) and with 2.3 (46.6 ka) and 2 precession cycles (40.8 ka) in B2b to E are present. Other peaks that exceed at least the 95% CI with periods of 11, 8 and 3.6 precession cycles in segment B1-B2a (66.44 – 118.52m) and with 13, 9.7, 4 and 2.7 precession cycles in B2b-E (120.02 – 178.12 m) could not be related to any orbital signal (Fig. 12a, Tab. 2).

The Redfit analysis of the Fe data (Fig. 12b) shows peaks that can be linked to a 405 ka eccentricity influence and exceed the 99% CI at period lengths of 7.6 m (413 ka) in the lower parts of the Postalm section (66.44 – 118.52m, B1 -B2a) and 7.7 m (409 ka) in the upper parts of the outcrop B2b-E (120.02 – 178.12 m). Signals at 16 m (90 ka) the segment from 66.44 – 118.52m (B1 -B2a) and at 2.4 m (127 ka) and 1.58 m (83 ka) in B2b-E (120.02 – 178.12 m) correspond to the 96 ka or 126 ka eccentricity cycles (see Laskar et al. 2004, 2011). The latter barely reaches the 90% CI. In segment B1-B2a (66.44 – 118.52m) peaks at 0.9 (49 ka) and 0.8 (44 ka), and in B2b-E (120.02 – 178.12 m) at 0.9 m (44 ka) barely exceed the 95% CI and might correlate to obliquity frequencies. Harmonic signals with period lengths of 0.5 m (27 ka) and 0.47 m (23.9 ka) in B1-B2a (66.44 – 118.52m), and 0.5 m (23 ka) and 0.43 m (19 ka) in B2b-E (120.02 – 178.12 m) exceed the 99% CI and likely represent precession signals. Peaks with period lengths of 5.56 m (247 ka) and 1.2 m (66 ka) are evident in segment B1-B2a (66.44 – 118.52m), and a faint signal at 1.58 m (83 ka) is present in B2b-E (120.02 – 178.12 m). These signals cannot be correlated to an orbital target curve and/or do not exceed the 90% CI (Fig. 12b, Tab. 2).
Stable $\delta^{13}C$ values show evidence of short frequency cycles; Redfit spectrograms display peaks at 17 m (933 ka in B1-B2a) and 23 m (1200 ka in B2b-E). A faint signal with a period length of 8.5 m (466 ka) is present at B1-B2a (66.44 – 118.52m) marked by a spectral peak of a 933 ka signal. A conspicuous peak corresponding to the 405 ka eccentricity (E1) cycle is present in B2b-E (120.02 – 178.12 m) at 8.3 m (430 ka). Periods corresponding to “short” eccentricity cycles (e2 with ~120 ka and e3 with ~90 ka) are not well expressed in Redfit spectral analyses of the $\delta^{13}C$ data. Two peaks that exceed the 90% CI are present in B1-B2a (66.44 – 118.52m) at 2 m (113 ka) and 1.8 m (98 ka). In segment B2b-E (120.02 – 178.12 m) two peaks do not reach the 90% CI but correspond to variations of the 100 ka eccentricity cycle, i.e., at 2.4 m (125 ka) and 2 m (105 ka). In the older part of the Postalm section evidence of cycles with period lengths of 0.98 m (51 ka) and 0.76 m (41 ka) was found that correspond to obliquity terms. In segment B2b-E (120.02 – 178.12 m) peaks at 0.8 m (37 ka) and 0.6 m (30 ka) correspond to obliquity, and a peak at 0.4 m (20 ka) could represent a precession signal. In this section a moderately significant signal (barely exceeding the 95% CI) with 1 m (55 ka) is also present that cannot be correlated to an orbital target (see Fig. 12c, Tab.2).

################figure 12

################ table 2

4.7.2. Evolutive Harmonic Analysis

EHA was performed on the $\delta^{13}C$, the Fe and the L/M thickness data in segments B1-B2a (66.44 – 118.52m) and B2b-E (120.02 – 178.12 m). This windowed Fourier analysis allows following the behaviour of spectral signatures through time (see Fig. 13).

An EHA of the $\delta^{13}C$ data reveals strong evidence of harmonic frequencies that correlate to the 405 ka eccentricity cycle (E1 cycle). This highly significant signal is continuously present and does show changes in sedimentation rate as the signal fluctuates between frequencies of 0.001 and 0.003 in the lower segment and between 0.001 and 0.002 in the overlying strata.

The Fe data show a discontinuously significant signal corresponding to the E1 cycle. In the older strata B1-B2a (66.44 – 118.52m), between 93 and 103 m, the dominant long-term harmonics shift from a signal that can be attributed to the E1 cycle to a higher frequency that might attribute to an obliquity influence. The harmonics in Fe values behave similarly in the upper part of the Postalm section. A well expressed, highly significant signal corresponding to the E1 cycle seems to be interrupted between 135 and 140 m, and between 154 and 153 m. In these intervals a strong influence of higher frequency harmonics was observed that could be attributed to an obliquity influence. Up section dominant harmonics fluctuate between E1 and 120ka (E2) The EHA of Fe values revealed signals that could represent the influence of orbital precession. The latter are not very well expressed and seem to be visible only upon changes in the sedimentation rate. Harmonics with higher frequencies between 0.020 and 0.025 appear also in the Redfit analyses and are close to the Nyquist frequency.

The L/M record shows discontinuous evidence of the three eccentricity cycles (E1, E2 and 90ka E3) and a prominent signal at 0.1 frequency (~220 ka) in segment B1-B2a, and at 0.1 frequency (~247 ka) in B2b-E that cannot be attributed to an orbital signal. Evidence for obliquity signals is present in both segments.

################figure 13

4.7.3. Bandpassing L/M, Fe and $\delta^{13}C$ data

Seventeen full (405 ka) long-eccentricity cycles have been reconstructed in the L/M data series (8 or 8.5 in B1-B2a, 66.44 – 118.52m, and 9 in B2b-E, 120.02 – 178.12 m) and accordingly also 17 cycles both in $\delta^{13}C$ (8.5 in the older and 8.5 in the younger profile segment) and in Fe (8.5 and 8.5, Fig. 14). Therefore, these three independently assessed data series show similar durations according to the cyclostratigraphic assessment (focussing on the 405 ka cycle). However, we found 30 100 ka-cycles in the L/M data, and 27 in the Fe and $\delta^{13}C$ data in segment B1-B2a, 66.44 – 118.52 m and 32 100 ka-cycles in the L/M data, and 28 in Fe and $\delta^{13}C$ in the younger profile segment B2b-E, 120.02 – 178.12 m.

4.7.4. Orbital tuning and correlation to the Laskar solution

We attempted tuning the $\delta^{13}C$ and Fe data to the spectral drift of the 405 ka cycle and subsequently correlating the model to the Laskar solution 2010 a (Laskar et al., 2011). This solution provided the basis for the astrochronological dating of the Maastrichtian and late Campanian by Husson et al. (2011). Figure 16 shows a possible astrochronologic solution for the Postalm section.

The tuned Fe and $\delta^{13}C$ signature show approximately 7 405 ka and 29 100 ka cycles between 66.44 – 118.52 m (B1-B2a), 11 405 ka-cycles and 44 100 ka-cycles from 120.02 – 178.12 m (B2b-E), and 43-45 cycles for the $\delta^{13}C$ data. Two and a half 405 ka cycles are interpolated through a likely discontinuity right below the magnetic reversal evident in the lowermost strata of section PE. The Laskar orbital solution correlates negatively with $\delta^{13}C$ and positively with Fe. In the tuned dataset, the maximum excursion of what is interpreted as the LCE is recorded at approximately 74.91 Ma.

#############fig.15

Discussion

5.1. Magnetostratigraphy

The palaeomagnetic reversal from Chron C34n to C33r is recorded between 2.66 and 2.81 m, in close vicinity to bioevents marking the Santonian/Campanian transition; such as the HO of the planktonic foraminiferal marker taxon *D. asymetrica*, and the LO of the nannofossil *B. parca parca*. A detailed discussion and elaborate study of the palaeomagnetic reversal and bioevents of the Santonian/Campanian boundary at the Postalm section (at ~2.7m) can be found in Wolfgring et al. (2018).

Most parts of the section show a normal polarity, that can be attributed to Chron C33n in accordance with bio- and isotope stratigraphy. The single reverse sample at 75.55 m (PT118) towards the base of C33n is of high-quality. This sample is embraced by normal samples at 73.56 m and 76.24 m. No short geomagnetic feature has been documented to our knowledge within the relatively long chron C33n. Consequently, the potential occurrence of such short reversal or geomagnetic excursion deserves further research in the future.

The reversal at 165.12m is located just above a fault or discontinuity in between sections D and E. Assuming that this short reversal represents the top of Chron C32r.1r, we postulate a gap in the record between sections D and E.

5.2. Biostratigraphy

5.2.1. Foraminifera biostratigraphy

The planktonic foraminifera of the Postalm section represent a typical Tethyan Campanian planktonic foraminiferal community. Cosmopolitan, small, simple planispiral and biserial planktonic foraminiferal taxa dominate the 63 to 500 µm fraction, larger, more complex planktonic forms are rare (see Wolfgring and Wagreich, 2016, for a more detailed quantitative analysis of the planktonic foraminiferal communities in the *R. calcarata* Zone at the Postalm section).

From the seven planktonic foraminiferal zones identified at the Postalm section only three are considered complete: the *Radotruncana calcarata* Zone, the *Globotruncanella havanensis* Zone and the *Globotruncana aegyptiaca* Zone. The *Dicarinella asymetrica* Zone is present in the lowermost segments at the section. Yet, the Santonian part recorded in the Bibereck Formation (underlying the Nierental Formation in this outcrop) only covers the uppermost segment of this biozone. The Santonian/Campanian boundary is placed near the top of the *Dicarinella asymetrica* Zone, at the magnetic reversal from C34n to C33r (for a detailed assessment of this interval the reader is referred to Wolfgring et al., 2018).

The record of the *Globotruncanita elevata* Zone is limited by a poor outcrop situation in the lower parts of the Postalm section. An early Campanian age can be assigned for this interval. The same situation applies to the *Contusotruncana plummerae* Zone. The index taxon is also extremely rare at the Postalm section. This is the reason why we still refer to the *Globotruncana ventricosa* Zone in our biostratigraphic interpretation (this zone is now obsolete; the reader is referred to Petrizzo, 2011, regarding the difficulties in identifying this planktonic foraminiferal zone). This interval covers parts of the mid-Campanian (according to Ogg et al., 2012).

The following *Radotruncana calcarata* Zone exhibits a completely undisturbed record that can be safely correlated to other Tethyan sections and was astronomically calibrated (Wagreich et al., 2012, Wolfgring et al., 2016).

The overlying *Globotruncanella havanensis* and *Globotruncana aegyptiaca* zones are less reliable markers due to the apparent diachroneity of the index taxa and the inconsistent identification of their base ages (e.g., Huber, 2008; Voigt et al., 2012). The uppermost planktonic foraminiferal zone identified at the Postalm section is the *Gansserina gansseri* Zone. A late Campanian age is interpreted for the topmost part of the section. This is also supported by the FO of rugoglobigerinid taxa in the topmost strata. A single specimen that was identified as *Racemiguembelina* sp. cf. *R. powelli* was recorded in the topmost section part (PE 26). *Racemiguembelina powelli* is known from the uppermost Campanian *G. gansseri* Zone (e.g.: Coccioni and Premoli Silva, 2015).

5.2.2. Nannofossil biostratigraphy

Nannofossils show assemblages typical of the low-latitude Tethys throughout the section with a dominance of *Watznaueria barnesa*e and the occurrence of other generally warm-water taxa like *Ceratolithoides* and *Uniplanarius*. A small number of cooler water taxa (Burnett, 1998; Thibault et al., 2016) such as *Kamptnerius, Monomarginatus, Biscutum* cf. *magnum* and *Gartnerago* spp. occurs sporadically within the section and attest to more marginal palaeobiogeographic position with some cooler-water influence, but do not define distinct cooling events in the investigated time interval.

The applied zonation relates to the Tethyan-intermediate province of Burnett (1998) and the CC zones of Sissingh (1977) and Perch-Nielsen (1985). However, some markers are not present in the Postalm section, like *Bukryaster hayi, Misceomarginatus pleniporus* and *Ceratolithoides arcuatus*.

The base of the section in nannofossil zone UC13 is regarded as late Santonian in age, below the LO of *Broinsonia parca parca* (base of UC14a) shortly above the magnetic reversal from C34n to C33r (Wolfgring et al., 2018). Zones UC14b to UC15a are not fully represented because of the rather poor outcrop situation between 13 and 66.44 m.

The mid-Campanian starts close to the LO of *Ceratolithoides aculeus* at the base of nannofossil zone UC15b (Ogg et al., 2012) and the late Campanian starts near the LO of *Uniplanarius trifidus* at the base of UC15d.

The top of the Postalm section belongs to UC16 above the HO of both *Eiffellithus eximius* and *Reinhardtites anthophorus*. *Broinsonia parca constricta*, *Uniplanarius trifidus* and *Tranolithus orionatus* are present up to the top of the section. This defines the nannofossil zones UC16 and CC23a where the Campanian-Maastrichtian boundary is situated (Küchler et al., 2001; Wagreich et al., 2003; Thibault et al., 2016). However, there is no indication that the section extends into the Maastrichtian, thus a late Campanian age for the uppermost part is highly likely also based on nannofossil biostratigraphy.

5.2.3. Age-depth model

The age-depth model presented in Figure 8 shows a generally good agreement with the planktonic foraminiferal dates. Comparing the Postalm section the the classical Tethyan section of Gubbio, we find major differences in the position of *Globotruncana atlantica* and *Pseudoguembelina carseyae.* A possible explanation for the poor fit of *G. atlantica* in the age-depth model is the poor outcrop situation and, thus, the poor recovery of the lower Campanian in the older segments of the Postalm section. An approximately 30 m-thick interval underlying segment

B1 is not exposed, thus the LO dates of microfossils in this part are uncertain.

The LO of *Pg. carseyae* is based on a broken specimen (*Pseudoguembelina* sp. cf *Pseudoguembelina carseyae*, recovered at 167.9 m) and therefore should be considered only as a biostratigraphic hint rather than an indicator of a zonal age.

The nannofossil markers follow the age-depth trend of the foraminifera with two exceptions: the LO of *Ceratolithoides* cf. *verbeekii* and the HO of *Eiffellithus exiumius* are older than expected. The precise levels of both bioevents are compromised by the scarcity of taxa in the samples. *Ceratolithoides* cf. *verbeekii* was often found after the LO of

Broinsonia parca constricta; however, such morphotypes do rarely occur below this bioevent (e.g., Melinte-Dobrinescu and Bojar 2010). The HO of *Eiffellithus exiumius* is also a rare event and may be blurred by reworking. The position of the palaeomagnetic reversal between chrons C32n.2n and C32r.1r at 73.6 +-0.08Ma (Husson et al., 2011) blends well with the micro- and nannofossil ages.

Given the good linear fit of the Postalm age-model to complete successions of the Campanian elsewhere we do not expect significant large-scale disturbances in most of the Postalm section (possibly apart for the covered intervals at the base Campanian from 13.09 to 45.29 m and 47.79 to 66.44 m. The foraminiferal and nannofossil record, however, display few calibrated marker taxa towards the uppermost Campanian as compared to Coccioni and Premoli Silva (2015) and Scott (2014).

5.3. Strontium isotopes

The Sr isotope data of the Postalm section match the marine Sr isotope reference curve for the Upper Cretaceous (McArthur et al., 1994, 2001). There is no evidence of a major hiatus. The $^{87}Sr/^{86}Sr$ value of subsection A exceeds the value for the Santonian/Campanian boundary from the Western Interior (McArthur, 1994). It is not possible to directly correlate and compare the sample points of Postalm to other $^{87}Sr/^{86}Sr$ datasets in regard to the exact stratigraphic position of samples. Nevertheless, the Sr isotope signature recorded at Postalm roughly matches the trend recorded in the composite $^{87}Sr/^{86}Sr$ dataset for the Campanian (McArthur et al., 2012) and displays similar $^{87}Sr/^{86}Sr$ values as documented in Sinnesael et al. (2019).

5.4. Fe stratigraphy

The Fe content in pelagic rocks typically mirrors changes in the carbonate/clay ratio. A decrease in carbonate content is thus mirrored by higher Fe concentrations as the latter reflect the amount of terrigenous input (e.g., Westerhold et al., 2017; Batenburg et al., 2017; Westerhold and Röhl, 2009).

The increase in Fe content towards the top of the Postalm section correlates with an increase in turbidite frequency in the upper part of the section (from 155.8 m to the top of the section), as the Fe is associated with terrigenous sediment influx. Changes in the Fe concentration represent variations in the terrigenous sediment delivery – an increase is likely to correlate to increasing turbidity current activity reflecting an increased runoff from – and sedimentation at the continental margin.

A possible driver behind cyclic patterns in Fe concentrations could be found in variations in redox conditions documented at the Postalm section. Carbonate associated Fe was found to mostly indicate suboxic conditions (see Neuhuber et al., 2016 for a thorough documentation). Neuhuber et al. (2016) identified several oxic phases during the *R. calcarata* Zone at Postalm. Low carbonate associated Fe values might be linked to oxic phases that could be caused by changes in regional currents or subtle sea-level fluctuations. The (mostly) inverse phase relationship of $\delta^{13}C$ and Fe could also be explained by alternating nutrient rich and oxic conditions documented at the Postalm section.

5.5. Carbon isotope stratigraphy

The most prominent excursion in the Postalm section is interpreted as the Late Campanian Event (LCE, Jarvis et al., 2006). In addition, there are indications of the Santonian-Campanian Boundary Event (SCBE) (Wolfgring et al., 2018). A more detailed look and correlations with biostratigraphy and palaeomagnetic data, however, reveal some uncertainty in the timing of both rather distinct carbon isotope events, as well as a possible diachroneity of microfossil dates (see Wolfgring et al., 2018).

The LCE remains an unreliable marker for a detailed correlation because it is either recorded within or after the distinct and short (~800 ka) *R. calcarata* Zone. Wendler (2013) places the LCE at 75.51 Ma, Thibault et al. (2012) constrained the duration of the LCE in ODP Hole 762C to 0.44 Ma (from 74.96 to 75.4 Ma) and Voigt et al. (2012) calibrated carbon isotope signatures of northern German sections, the English Chalk sections as well as Gubbio, Tercis and the Stevns-1 borehole and found the peak of the LCE at 75.4-75.6 Ma. An astronomical calibration of the LCE in the North Sea by Perdiou et al. (2015) places the LCE eight 405 ka-eccentricity cycles below the Campanian Maastrichtian boundary (at around 75.5 Ma) similar to observations by Chenot et al. (2016; 2018) in the Aquitaine and Paris basins. The most prominent carbon isotope excursion recorded in the upper Campanian of the Postalm section (at ~158m) lies above the known positions of the LCE between ~ 74.9-75.3 Ma (Voigt et al., 2012; Thibault, et al., 2012; Wendler, 2013) and slightly above the range of 8 405 ka-cycles of Perdiou et al. (2015) if we follow the orbital solution (option 1) of Husson et al. (2011) and use the top of the *R. calcarata* Zone as a tie point (Fig. 15).

The negative excursions recorded in the uppermost intervals of the section (top of segment PE) could possibly be related to the negative trend in the $\delta^{13}C$ curve that is observed at the Campanian-Maastrichtian Boundary Event (CMBE, Voigt et al., 2012; Wendler, 2013). There is no evidence for a longer lasting distinct negative trend in the isotopic signature, however, It is likely that the $\delta^{13}C$ record at the Postalm section terminates just before the CMBE (with a position around mid-Chron C32n.2n, Voigt et al., 2012).

5.6. Cyclostratigraphy

5.6.1. Resolution of cyclostratigraphic data

The three independently assessed proxies show differences in spectral resolution both in the EHA and the Redfit analyses. The L/M record was sampled at a “per-precession cycle” resolution, thus the obliquity signal is the highest orbital term that can be expressed in spectral resolution (see 4.6.2). The Fe time series shows the highest sample resolution. Only in this dataset we find signals that can undoubtedly be attributed to precession terms. The $\delta^{13}C$ record displays a weak precession signal in the younger segment of the Postalm section.

As visualized in the EHA, dominantly low-frequency orbital cycles fluctuate between the 405 ka-long E1 and the shorter 120 and 90 ka-long E2 and E3 signals. An obliquity influence is evident in both profile segments, but stronger in the older part of the section.

5.6.2. Trends in cyclostratigraphic data

Although we found the highest sample resolution and density in the Fe dataset, the carbon isotope curve is the only proxy time series showing explainable long-term harmonics. A weak indication of a 1-1.2 Ma cycle is shown by Redfit analyses in both segments. The signal for a longer term $\delta^{13}C$ cycle is not clearly expressed between 66.44 – 118.52 m and is masked and/or amalgamated by what seems to be an eccentricity variation or superimposed eccentricity cycles with a peak around ~950 ka. In the younger segment of the Postalm section (between 120.02 – 178.12m), a peak corresponding to a 1.2 Ma signal barely reaches the 95% CI (Fig. 11 and Tab. 2). Both signals are not visible in the EHA. Nevertheless, we interpret these signals to reflect the 1.2 Ma obliquity signal, as the display window of the Redfit analysis has, in comparison to the EHA, a better resolution of low frequencies.

An astronomical pacing of the global carbon cycle during the Late Cretaceous was emphasized by Batenburg et al. (2014), Wendler et al. (2014), Laurin et al. (2014) for the 1.2 Ma cycle, and by Martinez et al. (2015) for a long-term variation in carbon flux of 9 Ma. The 1.2 Ma obliquity variation can be possibly linked to 3rd order cycles, longer term climate variability and sea-level fluctuations (e.g., Lourens and Hilgen, 1997; Levrard and Laskar, 2003; Li et al., 2018; studies that specifically discuss influence of the 1.2 Ma obliquity cycle during the Late Cretaceous include Wendler et al., 2014 and Laurin et al., 2014). A cyclostratigraphic constrained duration close to 1.2 Ma duration of previously described 3rd order depositional sequences in Late Cretaceous of the Basque Basin was linked to long-period obliquity influence on sea-level (Dinarès-Turell et al., 2012).

The Fe data rather reflect short(er) term changes in the climate system. The paleogeographic setting of the Postalm section on an active continental margin, few tens of kilometres from the shore (Wagreich and Faupl, 1994), makes the Fe record a valuable archive. Fe is used as proxy for variations in terrigenous sediment delivery, aeolian dust input, carbonate productivity and to calculate climate cycles as it can be used to trace climatic variations that influenced the source and amount of detrital material transported into the basin (Röhl and Abrams, 2000; Westerhold et al., 2008; Röhl et al., 2001, Sinnesael, et al., 2018; also see Croudace and Rothwell, 2015 for a detailed review). An increase in the concentration of the detrital element Fe could therefore be an indicator for increased weathering and runoff in the uppermost parts of the Postalm section. This is also reflected in increased turbidite activity (which could be attributed to local tectonic events) towards the top of the section which supports the link between Fe and terrigenous sediment input. This hypothesis also explains the inverse phase relationship of the Fe and $\delta^{13}C$ datasets. Periods of increased weathering could be linked to periods with higher precipitation and therefore lower $\delta^{13}C$ values.

5.6.3. Orbital tuning and fit to the Laskar solution

The orbitally tuned records of $\delta^{13}C$ and Fe result in a better resolved 405 ka signal with a similar duration as observed in the "untuned" data. We tentatively correlated the results of the orbital tuning of the Postalm sections $\delta^{13}C$ and Fe data to the Laskar 2010a solution (Laskar et al., 2011) to investigate the correlation between geochemical data and solutions for the upper Campanian of Husson et al. (2011) (see Fig. 15). We chose the top of the *R. calcarata* Zone, the position of the LCE and the overlap and correlation of Fe and $\delta^{13}C$ data to the Laskar curve as points of reference. We are aware that this is a somehow arbitrary approach considering that there are different scenarios for the top of *R. calcarata* Zone that depend on different orbital solutions for the Campanian-Maastrichtian transition and in the following the duration of the Maastrichian and the position of the K/Pg boundary (Husson et al., 2011). Two possible solutions for the top of the *R. calcarata* Zone were published in Wagreich et al. (2012). After a cyclostratigraphic assessment and an evaluation of the $\delta^{13}C$ record, we consider the most likely solution for the top of this biozone to be about 74.6 Ma (Fig. 15, top *R.c.* solution 1).

Figure 15 documents the calibration of the Postalm section to the solutions of Husson et al. (2011) as well as a comparison to the cyclostratigraphic model of Voigt and Schönfeld (2010). In this model the top of the Postalm succession is calibrated by the top of magnetochron C32r.1r at about 165m (section 4.4).

We record the top of the Postalm section to be either synchronous with the topmost cycle of the Campanian (cycle Ca405^{1}) or the base cycle of the Maastrichtian (cycle number Ma405^{17}) of Husson et al. (2011). Following this approach, the number of 405 ka cycles between the maximum excursion of the prominent carbon isotope excursion that we interpret as a possible LCE and the Campanian/Maastrichtian boundary is not in accordance to the position published in the models of Voigt et al. (2012), Thibault et al. (2012) and Perdiou et al. (2015). The model illustrated in Figure 16 reconstructs six 405 ka cycles between the possible LCE and the Campanian/Maastrichtian boundary. Choosing different astrochronologic solutions for the position of the Campanian/Maastrichtian boundary or the position of the top *R. calcarata* results in +/- one 405 ka cycle.
The position of the older profile segment is constrained by the age for the base of magnetochron C33n (79.9 Ma according to Ogg, 2012).

5.6.4. Difference in time series data from three different proxies

The Fe data show a higher sample density and resolution than the carbon isotope data and the L/M data. However, it is not only the sampling resolution that affects the results of spectral analyses. A high resolution allows identifying higher frequencies in the EHA and Redfit analyses, which explains the differences in the results of the spectral analyses of the three proxies. A different number of eccentricity cycles present in spectral analyses of the L/M dataset might be attributed to the difficult identification of thin to missing marl layers, or such that are overprint by amalgamated strata packages of thick limestone layers, or prominent joints between two limestone layers (from weathered marls). In spectral analyses, misinterpretations of physical traits can result in erratic results for the combined thickness of limestone/marl layers, and thus in some inaccuracy in the number of precession cycles.

Furthermore, the comparison of the Fe and $\delta^{13}C$ data reveals a slight phase shift. This may reflect the slightly different positions and number of samples for XRF analyses and carbon isotopes. Only slightly different sample resolution within the two proxies can lead to disagreeing results in the tuned data series. We cannot rule out that differences in the cycle lengths of the 400 ka eccentricity between the Fe and $\delta^{13}C$ dataset cycle (see table 1) could be related to diagenetic alteration of the $\delta^{13}C$ data. Yet, we interpret the 405 ka signal of the three proxies to be robust; the three independently assessed proxies all result in a 405 ka eccentricity cycle with an average length of 8 m.

6. Conclusions

The multistratigraphic assessment of the Postalm section provides new insights into the bio-, chemo- and cyclostratigraphic framework of the Campanian in the Tethyan realm. This study shows that the 405ka cycle can be unambiguously identified even using non-ideal field data, represented by three different proxies from an active and slightly tectonised former Alpine continental margin succession.

1) The Sr isotope record matches the data for the Upper Cretaceous and suggests no major gaps in the Postalm succession.
2) Carbon isotope data allow the identification of the LCE and possibly the SCBE
3) Magnetostratigraphic and biostratigraphic data was linked to a floating astronomical timescale and help to refine Tethyan planktonic foraminifera and nannofossil zonations.
4) A robust cyclostratigraphic assessment of three independent data series (L/M

couplets, Fe and $\delta^{13}C$) resulted in the identification of eighteen 405 ka eccentricity cycles. The upper segment of the Postalm section was correlated to the Laskar 2010a solution (Laskar et al., 2011) using the position of the top of the *R. calcarata* interval, the position of the LCE and the top of Chron C32r.1r.

5) The floating astronomical timescale of the Postalm section adds to the cyclostratigraphic record of the upper Campanian and can be linked to the solution of Husson et al. (2011).

To refine the chronology of Late Cretaceous pelagic successions, more records with tie points that rely on absolute ages are needed. The lower Campanian requires more complete successions to refine biostratigraphic zonations and to tie them to absolute ages.

7. Acknowlegements

This research was funded by the Austrian Science Fund (FWF) project P240/44-N24, IGCP 609 and the International Programs of the Austrian Academy of Sciences. The authors thank David K. Watkins and an anonymous reviewer for their constructive remarks and valuable suggestions.

8.References

Batenburg, S.J., Friedrich, O., Moriya, K., Voigt, S., Cournède, C., Blum, P., Borneman, A., Fiebig, J., Hasegawa, T., Hull, P.M., Norris, R.D., Röhl, U., Sexton, P.F., Westerhold, T., Wilson, P.A. and the Expedition 342 scientists, 2018. Late Maastrichtian carbon isotope stratigraphy and cyclostratigraphy of the Newfoundland Margin (Site U1403, IODP Leg 342), Newsletters on Stratigraphy, 51, 2, 245-260.

Batenburg, S.J., Gale, A.S., Sprovieri, M., Hilgen, F.J., Thibault, N., Boussaha, M., Orue-Etxebarria, X. 2014. An astronomical timescale for the Maastrichtian based on the Zumaia and Sopleana sections (Basque country, northern Spain). Journal of the Geological Society, 171, 2, 165-180. DOI: 10.1144/jgs2013-015.

Berger, A., Loutre, M.F., Laskar, J., 1992. Stability of the astronomical frequencies over the Earth’s history fore paleoclimate studies. Science, 255, 560-566.

Blakey, R.C., 2016, Library of paleogeography; Colorado Plateau Geosystems, Inc., http://cpgeosystems.com (accessed may, 2018).

Bunn AG, 2010. Statistical and visual crossdating in R using the dplR library. Dendrochronologia, 28, 4: 251-258. ISSN 1125-7865

Bunn, A.G., Korpela, M., Biondi, F., Campelo, F., Mérian, P., Qeadan, F., Zang, C., 2016. dplR: Dendrochronology Program Library in R. R package version 1.6.4. http://R-Forge.R-project.org/projects/dplr/

Burnett, I., 1998. Upper Cretaceous. In: Brown, P.R. (ed.) Calcareous Nannofossil Biostratigraphy, Chapman and Hall, Cambridge, 132-199pp.

Chenot, E., Pellenard, P., Martinez, M., Deconinck, J.-F., Amiotte-Suchet, P., Thibault, N., Bruneau, L., Cocquerez, T., Laffont, R., Pucéat, E., Robaszynski, F., 2016. Clay mineralogical and geochemical expressions of the "Late Campanian Event" in the Aquitaine and Paris basins (France): Palaeoenvironmental implications. Palaeogeography, Palaeoclimatology, Palaeoecology, 447, 42-52.

Chenot, E., Deconinck, J-F., Pucéat, E., Pellenard, P., Guiraud, M., Jaubert, M., Jarvis, I., Thibault, N., Cocquerez, T., Bruneau, L., Razmjooei, M., Boussaha, M., Richard, J., Sizun, J-P., Stemmerik, L., 2018. Continental weathering as a driver of Late Cretaceous cooling: new insights from clay mineralogy of Campanian sediments from the southern Tethyan margin to the Boreal realm. Global and Planetary Change, 162, 292-312.

Coccioni, R., Premoli Silva, I., 2015. Revised Upper Albian – Maastrichtian planktonic foraminiferal biostratigraphy and magnetostratigraphy of the classical Tethyan Gubbio section (Italy). Newsletters on Stratigraphy, 48/1, 47-90.

Dinarès-Turell, J., Pujalte, V., Stoykova, K. y Elorza, J. 2013. Detailed correlation and astronomical forcing within the Upper Maastrichtian succession in the Basque Basin. *Boletín Geológico y Minero,* 124 (2): 253-282.

Eldrett, J. S., Ma C., Bergman, S. C. Lutz B., Gregory, J., Dodsworth, P., Phipps M., Hardas P., Minisini, D., Ozkan, A., Ramezani, J., Bowring, S. A., Kamo, S. L., Ferguson, K., Macaulay, C., Kelly, A.E., 2015. An astronomically calibrated stratigraphy of the Cenomanian, Turonian and earliest Coniacian from the Cretaceous Western Interior Seaway, USA: Implications for global chronostratigraphy. Cretaceous Research 56, 316-344.

Gebhardt, H., Friedrich, O., Schenk, B., Fox, L., Hart, M., Wagreich, M. 2010. Paleoceanographic changes at the nothern Tethyan margin during the Cenomanian-Turonian Oceanic Anoxic Event (OAE-2). Marine Micropaleontology, 77, 25-45.

Gradstein, F.M., Ogg, J.G., Schmitz, M., Ogg, G., 2012. The geologic time scale 2012. Elsevier, Amsterdam.

Hammer, Ø., Harper, D.A.T., Ryan, P.D., 2001. PAST: Paleontological statistics software package for education and data analysis, Palaeontol. Electron. 4, 1, 9pp.

Handy, M.R., Schmid, S., Bousquet, R., Kissling, E., Bernoulli, D., 2010. Reconciling plate-tectonic reconstructions of Alpine Tethys with the geological record of spreading and subduction in the Alps. Earth-Science Reviews 102,121-158.

Hay, W. W., Flögel, S., 2012. New Thoughts about the Cretaceous Climate and Oceans. Earth Science Reviews, 115, 4, 262-272.

Hennebert, M., Robaszynski, F., Goolaerts, S., 2009. Cyclostratigraphy and chronometric scale in the Campanian – Lower Maastrichtian: the Abiod Formation at Ellès, central Tunisia. Cretaceous Research 30, 325–338.

Herbert, T.D., Gee, J., DiDonna, S., 1999. Precessional cycles in Upper Cretaceous pelagic sediments of the South Atlantic: Long-term patterns from high frequency climate variations. In: Barrera, E., Johnson, C.C. (Eds.). Evolution of the Cretaceous Ocean-Climate System, 332.

Herbert, T.D., Premoli Silva, I., Erba, E., Fischer, A.G., 1995. Orbital chronology of Cretaceous- Paleogene marine strata. SEPM Special Publication 54, 81-93.

Hilgen, F.J., Hinnov, L.A., Abdul Aziz, H., Abels, H.A., Batenburg, S., Bosmans, J.H.C., De Boer, B., Hüsing, S.K., Kuiper, K.F., Lourens, L.J., Rivera, T., Tuenter, E., Van De Wal, R.S.W., Wotzlaw, J-F., Zeeden, C., 2015. Stratigraphic continuity and fragmentary sedimentation: the success of cyclostratigraphy as part of integrated stratigraphy. In: Smith, D.G., Bailey, R.J., Burgess, P.M., Fraser, A.J. (eds), Strata and Time: Probing the Gaps in Our Understanding. Geological Society, London, Special Publications, 404.

Hinnov, L. A., 2012. Cyclostratigraphy and its revolutionizing applications in the earth and planetary sciences. GSA Bulletin, 125, 11-12, 1703-1734.

Hofer, G., Draganits, E., Wagreich, M., Hofmann, C-C., Reichenbacher, D., Grundtner, M-L., Bottig, M., 2011. Stratigraphy and geochemical characterisation of Upper cretaceous non-marine cycles (Grünbach Formation, Gosau Group, Austria) Austrian Journal of Earch Sciences 104(2):90-107.

Hohenegger, J., Coric, S., Khatun, M., Pervesler, P., Rögl, F., Rupp, C., Selge, A., Uchman, A., Wagreich, M., 2008. Cyclostratigraphic dating in the Lower Badenian (Middle Miocene) of the Vienna Basin (Austria) – the Baden-Sooss core. Internat. J. Earth Sci., doi 10.1007/s00531-007-0287-7.

Hohenegger, J., Wagreich, M., 2012. Time calibration of sedimentary sections based on insolation cycles using combined cross-correlation: dating the gone Badenian stratotype (Middle Miocene, Paratethys, Vienna Basin, Austria) as an example. International Journal of Earth Sciences (Geologische Rundschau), 101, 339-349.

Hu, X., Wagreich, M., Yilmaz, I.O., 2012. Marine rapid environmental/climatic change in the Cretaceous greenhouse world. Cretaceous Research 38, 1-6.

Hu, X, Jansa, L., Wang, C., Sartid, M., Bake, K., Wagreich, M., Michalik, J., Soták, J., 2005. Upper Cretaceous oceanic red beds (CORBs) in the Tethys: occurrences, lithofacies, age, and environments. Cretaceous Research, 26(1), 3-20.

Huber, B., MacLeod, K., Watkins, D., Coffin, M., 2018. The rise and fall of the Cretaceous Hot Greenhouse climate. Global and Planetary Change. 167. 10.1016/j.gloplacha.2018.04.004.

Husson, D., Galbrun, B., Laskar, J., Hinnov, L.A., Thibault, N., Gardin, S., Locklair, R.E., 2011. Astronomical calibration of the Maastrichtian (Late Cretaceous). Earth and Planetary Science Letters 305, 328-340.

Jarvis, I., Gale, A.S., Jenkyns, H.C., Pearce, M.A., 2006. Secular variation in Late Cretaceous carbon isotopes: a new δ13C carbonate reference curve for the Cenomanian-Campanian (99.6-70.6 Ma). Geological Magazine, 143, 561-608.

Jarvis I., Mabrouk A., Moody R.T.J., de Cabrera S., 2002. Late Cretaceous (Campanian) carbon isotope events, sea-level change and correlation of the Tethyan and Boreal realms. Palaeogeography, Palaeoclimatology, Palaeoecology. 2002;188:215–248.

Jarvis, I., Murphy, A.M., Gale, A.S., 2001. Geochemistry of pelagic and hemipelagic carbonates: criteria for identifying systems tracts and sea-level change. Journal of the Geological Society, London, 158, 685-696.

Jenkyns, H.C., Wilson, P.A., 1999. Stratigraphy, paloceanography, and evolution of Cretaceous Pacific guyots: relics from a greenhouse Earth. American Journal of Science, 299, 341-392.

Krenmayr, H.G., 1999. Die Nierental-Formation der Oberen Gosau-Gruppe (Oberkreide-Paläozän, Nördliche Kalkalpen) in Berchtesgaden: definition, fazies und environment. Jb. Geol. B.-A.141(4):409-447.

Krenmayr, H. G., 1996. Hemipelagic and turbiditic mudstone facies associations of the Upper Cretaceous Gosau Group of the Northern Calcalreous Alps (Austria), Sedimentary Geology 101:149-172.

Kirschvink, J.L., 1980. The least-squares line and plane and the analysis of palaeomagnetic data. Geophys. J. R. Astronom. Soc. 62, 699–718.

Laskar, J., Fienga, A., Gastineau, M., Manche, H., 2011. La2010: a new orbital solution for the long-term motion of the Earth. Astronomy and Astrophysics 532, A89. doi:10.1051/0004-6361/201116836.

Laskar, J., Robutel, P., Joutel, F., Gastineau, M., Correia, A.C.M., Levrard, B.,2004. A long term numerical solution for the insolation quantities of the Earth. A&A 428, 261-285 (2004), DOI: 10.1051/0004-6361:20041335.

Laurin, J., Meyers, S.R., Uličny, D., Jarvis, I., Sageman, B.B., 2014. Axial obliquity control on the greenhouse carbon budget through middle- to high latitude reservoirs. Paleoceanography, 30, 133-149, DOI: 10.1002/2014PA002736.

Levrard, B., Laskar, J., 2003. Climate friction and the Earth's obliquity. Geophysical Journal International, 154, 3, 970-990.

Li, M., Hnnov, L.A., Huang, C., Ogg, J.G., 2018. Sedimentary noise and sea levels linked to land-ocean water exchange and obliquity forcing. Nature Communications, 9/1004. DOI:10.1038/s41467-018-03454y.

Linnert, C., Robinson, S., Lees, J.A., Brown, P.R., Pérez-Rodríguez, I., Petrizzo, M.R., Falzoni, F., Littler, K., Arz, J.A., Russell, E.E., 2014. Evidence for global cooling in the Late Cretaceous. Nature Communications, 5:4194. DOI:10.1038/ncomms5194.

Liu, K., 2007. Sequence stratigraphy and orbital cyclostratigraphy of the Mooreville Chalk (Santonian-Campanian), northeastern Gulf of Mexico area, USA. Cretaceous Research 28, 405-418.

Loeblich Jr., A.R., Tappan, H., 1988. Foraminiferal Genera and their Classification. Van Nostelrand Reinhold Company, New York, 1-970.

Lourens, L.J., Hilgen, F.J., 1997. Long-periodic variation in the Earth's obliquity and their relation to third-order eustatic cycles and Late Neogene glaciations. Quat. Int., 40, 43-52.

Lowrie, W., J. E. T. Channell, and W. Alvarez (1980), A review of magnetic stratigraphy investigations in Cretaceous pelagic carbonate rocks, J. Geophys. Res., 85(B7), 3597–3605, doi: 10.1029/JB085iB07p03597.

Martinez, M., Dera, G., 2015. Orbital pacing of carbon fluxes by a ~9-My eccentricity cycle during the Mesozoic. PNAS, 112, 41, 12604-12609.

McArthur, J.M., Howarth, R.J., Shields, G.A., 2012. Chapter 7, Strontium Isotope Stratigraphy. In: Gradstein, F.M., Ogg, J.M., Schmitz, M.D., Ogg, G.M. (Eds.): The Geologic Time Scale, 2012, 1144pp, Elsevier, Amsterdam.

McArthur, J.M., Howarth, R.J., Bailey, T.R., 2001. Strontium isotope stratiography: LOWESS Version 3: best fit to the marine Sr- isotope curve for 0-509 Ma and accompanying look-up table for deriving numerical age. J. Geol. 109, 155-170.

McArthur, J.M., Kennedy, W.J., Chen, M., Thirlwall, M.F., Gale, A.S., 1994. Strontium isotope stratigraphy for Late Cretaceous time: Direct numerical calibration of the Sr isotope curve based in the US Western Interior. Palaeogeography, Palaeogclimatology, Palaeoecology, 108, 95-119.

Melinte-Dobrinescu, M.C., Bojar, A., 2010. Late Cretaceous carbon- and oxygen isotope stratigraphy, nannofossil events and paleoclimate fluctuations in the Haţeg area (SW Romania). Palaeogeography, Palaeoclimatology, Palaeoecology 293, 295–305.

Meyers, S.R., 2014. Astrochron: An R package for Astrochronology. http://cran.r-project.org/package=astrochron

Meyers, S.R., 2012. Seeing Red in Cyclic Stratigraphy: Spectral Noise Estimation for Astrochronology. Paleoceanography, 27, PA3228, Doi:10.1029/2012PA002307.

Meyers, S.R., Sageman, B. B., Hinnov, L. A., 2001. Integrated quantitative stratighraphy of the Cenomanian – Turonian bridge creek limestone member using evolutive harmonic analysis and stratigraphic modeling. Journal of Sedimentary Research, 71 (4), 628-644.

Nederbragt, A.J., 1991. Late Cretaceous biosotratigraphy and development of Heterohelicidae (planktonic foraminifera), Micropaleontology, 37, 329-372.

Neuhuber, S., Wagreich, M., Wendler, I., Spötl, C., 2007. Turonian oceanic red beds in the eastern Alps: concepts for palaeoceanographic changes in the Mediterranean Tethys. Palaeogeography, Palaeoclimatology, Palaeoecology, 251, 222-238.

Neuhuber, S., Gier, S., Hohenegger, J., Wolfgring, E., Spötl, C., Strauss, P., Wagreich, M., 2016. Palaeoenvironmental changes in the northwestern Tethys during the Late Campanian Radotruncana calcarata Zone: Implications from stable isotopes and geochemistry. Chemical Geology, 420, 280-296.

Ogg, J.G., Hinnov, L.A., Huang, C., 2012. Cretaceous. In: Gradstein, F.M., Ogg, J.M., Schmitz, M.D., Ogg, G.M. (eds.): The Geologic Time Scale, 2012, 1144pp, Elsevier, Amsterdam.

Ogg, J.G., 2012. Geomagnetic Polarity Time Scale. In: Gradstein, F.M., Ogg, J.M., Schmitz, M.D., Ogg, G.M. (eds.): The Geologic Time Scale, 2012, 1144pp, Elsevier, Amsterdam.

Perch-Nielsen, K., 1985. Cenozoic Calcareous Nannofossils. In: Bolli, H.M., Sanders, J.B. and Perch-Nielsen, K. (eds.), Plankton Stratigraphy, Cambridge University Press, Cambridge, 427-554

Perdiou, A., Thibault, N., Anderskouv, van Buchem, F., Buijs, G.JU.A., Bjerrum, C.J., 2015. Orbital calibration of the late Campanian carbon isotope event in the North Sea. Journal of the Geological Society, 173, 3, 504.

Petrizzo, M.R., Falzoni, F., Premoli Silva, I., 2011. Identification of the base of the lower-to-middle Campanian Globotruncana ventricosa Zone: Comments on reliability and global correlations. Cretaceous Research. 32. 387–405. 10.1016/j.cretres.2011.01.010.

Premoli Silva, I., Verga, D., 2004. Practical manual of cretaceous planktonic foraminifera. In: Verga, D., Rettori, R., eds. International school on Planktonic Foraminifera, Universities of Perugia and Milano. Perugia, Italy: Tipografie Pontefelcino. 283pp.

Premoli Silva, I., Sliter, W.V., 1995. Cretaceous Planktonic Foraminiferal Biostratigraphy & Evolutionary Trends from the Bottaccione Section, Gubbio, Italy. Palaeontographia Italica, 82, 1-89.

Pucéat, E., Lécuyer, C., Sheppard, S.M.F., Dromart, G., Reboulet, S., Grandjean, P., 2003. Thermal evolution of Cretaceous Tethyan marine waters inferred from oxygen isotope composition of fish tooth enamels. Paleoceanography 18, 1-12.

R Core Team, 2016. R: A language and environment for statistical computing. R foundation for Statistical Computing, Vienna, Austria. https://www.R-project.org/.

Robaszynski, F., Caron, M., 1995. Foraminiferes planktoniques du Crétacé: commentaire de la zonation Europe-Méditerranée. Bulletin de la Société Géologique de France 166:681-692.

Robaszynski, F., Mzoughi, M., 2010. The Abiod at Ellès (Tunisia): stratigraphies, Campanian-Maastrichtian boundary, correlation. Carnets de Géologie, 2010/4.Rothwell, R.G., Croudace, I., 2015. Micro-XRF Studies of Sediment Cores: A Perspective on Capability and Application in the Environmental Sciences. In: Croudace, I,W. and Rothwell, R.G, (eds.).Dordrecht, NL. Springer, pp. 1-20. (Developments in Paleoenvironmental Research, 17).

Sabatino, N, Meyers, S.R., Voigt, S., Coccioni, R., Sprovieri, M., 2018. A new high resolution carbon-isotope stratigraphy for the Campanian (Bottaccione Section): Its implications for global correlation, ocean circulation, and astrochronology. Palaeogeography, Palaeoclimatology, Palaeoecology, 489, 29-39.

Schulz, M., Mudelsee, M., Estimating red-noise spectra directly from unevenly spaced paleoclimatic time series. Computers and Geosciences. Computers & Geosciences, 28, 421-426.

Scott, R., 2014. A Cretaceous chronostratigraphic database: construction and applications. Carnets de Géologie (Notebooks on Geology), 14, 2.

Skelton, P. W., 2003. The Cretaceous World. Cambridge Univ. Press London, 360pp.

Sinnesael, M., de Winter, N., Snoeck, C., Montanari, A., Claeys, P., 2019. An integrated pelagic carbonate multi-proxy study using portable X-ray fluorescence (pXRF): Maastrichtian strata from the Bottaccione Gorge, Gubbio, Italy. Cretaceous Research. 91. 10.1016/j.cretres.2018.04.010.

Sinnesael, M., De Vleeschouwer, D., Zeeden, C., Batenburg, S. J., Da Silva, A-C., de Winter, N.J., Dinarès-Turell, J., Drury, A.J., Gambacorta, G., Hilgen, F.J., Hinnov, L.A., Hudson, A.L.J., Kemp, D.B., Lantink, M.L., Laurin, J., Li, M., Liebrand, D., Ma, C., Meyers, S.R., Monkenbusch, J., Montanari, A., Nohl, T., Pälike, H., Pas, D., Ruhl, M., Thibault, N., Vahlenkamp, M., Valero, L., Wouters, S., Wu, H., Claeys, P., 2019. The Cyclostratigraphy Intercomparison Project (CIP): consistency, merits and pitfalls, Earth-Science Reviews, 199, 102965, https://doi.org/10.1016/j.earscirev.2019.102965.

Sissingh W., 1977. Biostratigraphy of Cretaceous nannoplankton, with appendix by Prins B. & Sissingh W. *Geol. en Mijnb*., 56, 37-65.

Spötl, C., Vennemann, T., 2003. Continuous – flow isotope ratio mass spectrometric analysis of carbonate minerals. Rapid communications in Mass Spectrometry, 17, 9:1004-1006.

Stampfli, G.M., Borel, G.D., Marchant R., Mosar, J., 2002. Western Alps geological constraints on western Tethyan reconstructions. IK. In: G. Rosenbaum, G.S. Lister (Eds.), Reconstruction of the evolution of the Alpine–Himalayan Orogen, J. Virtual Explor., 7 (2002), pp. 75–104.

Strasser, A., Hilgen, F.J., Heckel, P.H., 2006. Cyclostratigraphy – concepts, definitions, and applications.

Thibault, N, Husson, D., Harlou, R., Gardin, S., Galbrun, B., Huret, E., Minoletti, F., 2012. Astronomical calibration of upper Campanian-Maastrichtian carbon isotope events and calcareous plankton biostratigraphy in the Indian Ocean (ODP Hole 762C) Implication for the age of the Camanian-Maastrichtian boundary. Palaeogeography, Palaeoclimatology, Palaeoecology, 337-338, 52-71.

Thibault, N., Harlou, R., Schovsbo, N.H., Stemmerik, L., Surlyk, F., 2016. Late Cretaceous (late Campanian-Maastrichtian) sea-surface temperature record of the Boreal Chalk Sea. Climate of the Past, 12, 429-438. DOI: 10.5194/cp-12-429-2016.

Thomson, D.J., 1982. Spectrum estimation and harmonic analysis. Proceedings of the IEEE, 70, 1055-1096.

Voigt, S., Gale, A.S., Jung, C., Jenkyns, H.C., 2012. Global correlation of Upper Campanian-Maastrichtian successions using carbon-isotope stratigraphy: development of a new Maastrichtian timescale. Newsletters on Stratigraphy, 45/1, 25-53.

Voigt, S., Schönfeld, J., 2010. Cyclostratigraphy of the reference section for the Cretaceous white chalk of northern Germany, Lägerdorf–Kronsmoor: A late Campanian–early Maastrichtian orbital time scale. Palaeogeography, Palaeoclimatology, Palaeoecology, 287, 67-80

Wagreich, M., 1993. Subcrustal tectonic erosion in orogenic belts—a model for the Late Cretaceous subsidence of the Northern Calcareous Alps (Austria) Geology 21:941-944.

Wagreich, M., 2012. “OAE 3” – regional Atlantic organic carbon burial during the Coniacian–Santonian. Climate of the Past, 8, 1447–1455, doi:10.5194/cp-8-1447-2012.

Wagreich, M., Neuhuber, S. 2005. Stratigraphy and geochemistry of an Early Campanian deepening succession (Bibereck Formation, Gosau Group, Austria). Earth Science Frontiers, 12, 123-131, Bejing.

Wagreich, M., Decker, K., 2001. Sedimentary tectonics and subsidence modelling of the type Upper Cretaceous Gosau basin (Northern Calcareous Alps, Austria) International Journal of Earth Sciences 90:714-726.

Wagreich, M., Hohenegger, J., Neuhuber, S., 2012. Nannofossil biostratigraphy, strontium and carbon isotope stratigraphy, cyclostratigraphy and an astronomically calibrated duration of the Late Campanian *Radotruncana calcarata* Zone. Cretaceous Research 38:80-96.

Wagreich, M., Krenmayr, H.G., 2005. Upper Cretaceous oceanic red beds (CORB) in the Northern Calcareous Alps (Nierental Formation, Austria): slope topography and clastic input as primary controlling factors. Cretaceous Research 1:57-64.

Wagreich, M., Faupl., P. 1994. Palaeogeography and geodynamic evolution of the Gosau Group of the Northern Calcareous Alps (Late Cretaceous, Eastern Alps, Austria). Palaeogeography, Palaeoclimatology, Palaeoecology, 110, 3-4. 235-254.

Wagreich, M., Egger, H., Gebhardt, H., Mohammed, O., Spötl C, Koukal V, Hobiger G, 2011. A new expanded record of the Paleocene-Eocene transition in the Gosau Group of Gams (Eastern Alps, Austria). Annalen des Naturhistorischen Museums in Wien A 113:35-65.

Weedon, G. P., 2003. Time - Series Analysis and Cyclostratigraphy: Examining Stratigraphic Records of Environmental Cycles, Cambridge Univ.Press, Cambridge, U. K,

Wendler, I., 2013. A critical evaluation of carbon isotope stratigraphy and biostratigraphic implications for Late Cretaceous global correlation. Earth-Science Reviews, 126, 116-146.

Wendler, J.E., Meyers, S., Wendler, I., Kuss, J., 2014. A million-year-scale astronomical control on Late Cretaceous sea-sevel. Newsletters on Stratigraphy, 47(1), 1-19.

Westerhold, T., Röhl, U., 2009. High resolution cyclostratigraphy of the early Eocene – new insights into the origin of the Cenozoic cooling trend, Clim. Past, 5, 309-327, https://doi.org/10.5194/cp-5-309-2009, 2009.

Westerhold, T., Röhl, U., Frederichs, T., Agnini, C., Raffi, I., Zachos, J.C., Wilkens, R.H., 2017. Astronomical calibration of the Ypresian timescale: implications for seafloor spreading rates and the chaotic behaviour of the solar system. Climate of the Past, 13, 1129-1152.

Wolfgring, E., Hohenegger, J., Wagreich, M., 2016. Assessing pelagic palaeoenvironments using formaminiferal assemblages – A case study from the late Campanian *Radotruncana calcarata* Zone (Upper Cretaceous, Austrian Alps). Palaeogeography, Palaeoclimatology, Palaeoecology, 441, 3, 467 -492.

Wolfgring, E., Wagreich, M., 2016. A quantitative look on northwestern Tethyan foraminiferal assemblages, Campanian Nierental Formation, Austria. PeerJ 4:e1757 https://doi.org/10.7717/peerj.1757

Wolfgring, E., Wagreich, M., Dinarès-Turell, J., Yilmaz, I.O., Böhm, K., 2017. Plankton biostratigraphy and magnetostratigraphy of the Santonian-Campanian boundary interval in the Mudurnu-Göynük Basin, northwestern Turkey. Cretaceous Research, in press, https://doi.org/10.1016/j.cretres.2017.07.006.

Wolfgring, E., Wagreich, M., Dinarès-Turell, J., Gier, S., Böhm., K., Sames, B., Spötl, C., Popp, F., 2018. The Santonian-Campanian boundary and the end of the Long Cretaceous Normal Polarity-Chron: Isotope and plankton stratigraphy of a pelagic reference section in the NW Tethys (Austria). Newsletters on Stratigraphy, 51, 4, 9, 445-476.

Young, J.R., Bown P.R., Lees J.A., 2017. Nannotax3 website. International Nannoplankton Association. Accessed 21 Apr. 2017. URL: http://www.mikrotax.org/Nannotax3

Zeeden, C., Meyers, S.R., Lourens, L.J., Hilgen, F.J., 2015. Testing astronomically tuned age models. Paleoceanography and Paleoclimatology, 30, 369-383.

Zijderveld, J.D.A., 1967. AC demagnetisation of rock: analysis of results. In: D.W. Collinson and others (eds.), Methods in palaeomagnetism. Elsevier, Amsterdam, 254–286.

.